



HAL
open science

State-to-state inelastic rate coefficients of phosphine in collision with He at low to moderate temperature

Ayda Badri, Faouzi Najjar, Cheikh Bop, Nejm-Eddine Jaidane, Majdi Hochlaf

► **To cite this version:**

Ayda Badri, Faouzi Najjar, Cheikh Bop, Nejm-Eddine Jaidane, Majdi Hochlaf. State-to-state inelastic rate coefficients of phosphine in collision with He at low to moderate temperature. *Monthly Notices of the Royal Astronomical Society*, 2020, 499 (2), pp.1578-1586. 10.1093/mnras/staa2611. hal-03078779

HAL Id: hal-03078779




<https://hal.science/hal-03078779>

Submitted on 16 Dec 2020

HAL is a multi-disciplinary open access archive for the deposit and dissemination of scientific research documents, whether they are published or not. The documents may come from teaching and research institutions in France or abroad, or from public or private research centers.

L'archive ouverte pluridisciplinaire **HAL**, est destinée au dépôt et à la diffusion de documents scientifiques de niveau recherche, publiés ou non, émanant des établissements d'enseignement et de recherche français ou étrangers, des laboratoires publics ou privés.

State-to-state inelastic rate coefficients of phosphine in collision with He at low to moderate temperature

Ayda Badri,^{1,2} Faouzi Najar,¹ Cheikh T. Bop,^{3,4} Nejm-Eddine Jaidane¹ and Majdi Hochlaf¹   

¹Laboratoire de Spectroscopie Atomique, Moléculaire et Applications LSAMA, Université de Tunis El Manar, Tunis, Tunisia

²Université Gustave Eiffel, COSYS/LISIS, 5 Bd Descartes, 77454 Champs sur Marne, France

³Laboratory of Atoms Lasers, Department of Physics, Faculty of Sciences and Techniques, University Cheikh Anta Diop of Dakar, Dakar 5005, Senegal

⁴LOMC-UMR 6294 CNRS, Université du havre, 25 rue Philippe Lebon, BP 1123, F-76063 Le Havre, France

Accepted 2020 August 20. Received 2020 August 19; in original form 2020 May 20

ABSTRACT

Several phosphorus-bearing molecules, such as the phosphine of interest here, have been detected in astrophysical media. With the aim of satisfying the precision required by the astrophysical community, we report the rate coefficients of PH₃ in collision with helium from low to moderate temperature. To this end, we constructed the first three-dimensional potential energy surface (3D-PES) of the PH₃–He van der Waals complex, which governs the nuclear motions. The 3D-PES was worked out by means of the standard coupled cluster with single, double and non-iterative triple excitation approach, in conjunction with the aug-cc-pVQZ basis set and complemented by mid bond functions. This 3D-PES presents a well of 34.92 cm⁻¹ at $\{R, \theta, \Phi\} = \{5.76a_0, 90^\circ, 60^\circ\}$. Afterwards, we incorporated this 3D-PES into time-independent close-coupling quantum dynamical computations to derive the inelastic cross-sections of rotational excitation of (ortho-) para-PH₃ after collision with He up to (1000) 500 cm⁻¹. Subsequently, we evaluated the rate coefficients for temperatures up to (100 K) 50 K populating the (41) 42 low-lying rotational levels of (ortho-) para-PH₃. These data were derived by averaging the cross-sections thermally over the Maxwell–Boltzmann velocity distribution. No general propensity rules are found. We also performed a comparison with the rates for NH₃–He. Differences are observed that invalidate the use of NH₃ rates for deducing accurate abundances of phosphine in cold astrophysical media. Our results should be of great help in determining accurate PH₃ abundances and, more generally, constraining the interstellar PH₃ chemistry better.

Key words: ISM : abundances – ISM: molecules.

1 INTRODUCTION

The second-row elements of the periodic table are present in the interstellar medium (ISM) with relatively low cosmic standards. Among them, phosphorous (known also as a biogenic element) is one of the less abundant. In fact, only one out of the 23 known nuclides of phosphorous is stable (³¹P), with a binding energy of ~8.4 MeV (Maciá 2005). However, its formation throughout thermonuclear fusion requires temperatures above 10⁹ K. Indeed, the barrier of electrostatic repulsion among the colliding nuclei related to a nuclear charge of $Z = 15$ (i.e. ³¹P formation) imposes a great amount of energy. These items let us expect that thermonuclear reactions leading to the formation of phosphorous can take place only in the cores of massive stars of size 15–100 M_⊙ (Arnett & Arnett 1996; Maciá 2005). For instance, the early origin of the ³¹P isotope occurred towards the inner zone of stars sufficiently massive to undergo successive carbon- and neon-burning at approximately $T = 3 \times 10^9$ K (Woosley 2002). Once produced in the cores of massive stars, this biogenic element is likely carried towards the ISM by supernova explosions (by the birth of planetary nebulae) in the case of very high-mass stars (of relatively high-mass stars) and stellar

winds. The stable phosphorus thus produced and liberated in the ISM would be ready to react with available atoms, leading to the formation of interstellar P-bearing compounds. Among them, phosphine, PH₃, of interest in the present work, is expected to be the main reservoir of phosphorous in space. Indeed, PH₃ has been observed in various astronomical environments over these last four decades (Moreno, Marten & Lellouch 2009; Weisstein & Serabyn 1996; Larson 1977; Bregman & Rank 1975). For instance, phosphine was definitely detected in several extraterrestrial environments. In the ISM, it was observed in the circumstellar envelope of the carbon star IRC+10216 (Agúndez et al. 2008; Tenenbaum & Ziurys 2008a). It is supposed to be formed on interstellar grains via successive hydrogenation of atomic phosphorus (Jiménez-Serra et al. 2018) and then desorbs to the gas phase. Phosphine was also identified in the atmospheres of Jupiter and Saturn (Ridgway, Wallace & Smith 1976; Larson et al. 1980). Thanks to the *Herschel* Spectral and Photometric Imaging Receiver (SPIRE), high-resolution far-IR observations of Saturn's atmosphere allowed us to determine the vertical distribution of PH₃. Moreover, this molecule is most likely present in the atmospheres of brown dwarfs or giant extrasolar planets (Sharp & Burrows 2007). Furthermore, it is connected to the origin of the phosphorus signal in comet 67P/Churyumov–Gerasimenko (Altwegg 2016).

In addition to PH₃, five other P-containing molecules, namely PN, PO, CP, HCP, CCP and NCCP, have been successfully detected in

* E-mail: hochlaf@univ-mlv.fr

interstellar and circumstellar regions (Turner & Bally 1987; Ziurys 1987; Guélin et al. 1990; Turner et al. 1990; Agúndez, Cernicharo & Guélin 2007; Halfen, Clouthier & Ziurys 2008; Milam et al. 2008). In terms of abundances, PH_3 and HCP , which are the dominant P-bearers in IRC+10216, hold only 2 (Agúndez et al. 2014) and 5 per cent (Agúndez et al. 2007) of atomic phosphorus, respectively. For other P-bearing compounds, the abundance ratio with respect to P drops to less than 0.001 (e.g. PN/P is about 5×10^{-4} ; Turner et al. 1990). Otherwise, gas-phase molecules in the envelopes of evolved stars lock a greater amount of phosphorus than in IRC+10216. Typically, in the carbon-rich envelope CRL 2668, HCP along with PH_3 holds about half the phosphorus (Milam et al. 2008; Tenenbaum & Ziurys 2008b), while a quarter of almost all the available phosphorus is in the form of PN and PO towards the oxygen-rich supergiant star VYCMa (Tenenbaum, Woolf & Ziurys 2007; Milam et al. 2008) or towards the star IK Tau (De Beck et al. 2013). These items are in concordance with the hypothesis of Turner et al. (1990), which was based on the weak presence of P-bearers in interstellar clouds, suggesting that phosphorus is depleted in dust grains. Nevertheless, chemical models for identification of the formation pathways of P-bearing molecules in astrophysical media suffer from the lack of accurate abundances for these species to assess the initial elemental abundance of phosphorus, which is connected with the depletion level of P (Chantzios et al. 2020).

For the identification of molecules in astrophysical media, one needs accurate determinations of line positions and abundances. For PH_3 , while its rotation–vibration spectrum is well-established theoretically and experimentally (Sousa-Silva et al. 2015), its abundance is not. Indeed, its abundance is estimated using the collision rates of isovalent ammonia. Therefore, accurately determining the abundances of phosphine may be a clue to understanding its formation and phosphorus chemistry in space.

In order to satisfy astrophysical precision when modelling the abundance of interstellar species observed in media where local thermodynamic equilibrium (LTE) conditions are not reached, one relies on the large velocity gradient approach (LVG). Such a procedure requires preliminary calculations of rate coefficients induced by collision with the most abundant species (H_2 , H and He), as well as Einstein coefficients. These latter are often known, while collisional rates are not. In the case of a lack of such data for a newly observed molecule, astrophysicists usually deduce its collisional rates from those of isoelectronic species. Indeed, this approximation has been adopted for some molecules (Barlow et al. 2013; Cernicharo et al. 2018) and its limits were pointed out thereafter (Bop et al. 2016). In the case of phosphine, the approximation made by Agúndez et al. (2014), who used the rate coefficients of NH_3 (Danby et al. 1988; Machin & Roueff 2005), could be *a priori* more reliable. Nevertheless, this hypothesis deserves to be checked by computing the actual PH_3 rate coefficients.

In this article, we investigate the rotational (de-)excitation of PH_3 colliding with He . Even if He is not the dominant collision partner in the ISM, the rate coefficients it yields may be used to evaluate those that would be obtained using para- H_2 ($j = 0$) as a projectile. Indeed, this approximation takes its suitability from the fact that para- H_2 ($j = 0$) is spherically symmetric and contains two valence electrons as helium. In addition, using helium as a projectile may be useful in the experimental framework for the interpretation of measured broadening parameters (Pickett, Poynter & Cohen 1981; Levy, Lacombe & Tarrago 1994; Salem et al. 2005). Therefore, we generated the first 3D potential energy surface (3D-PES) of the PH_3 – He van der Waals complex using the coupled cluster approach. This 3D-PES is mapped in Jacobi coordinates as defined in Fig. 1. Then

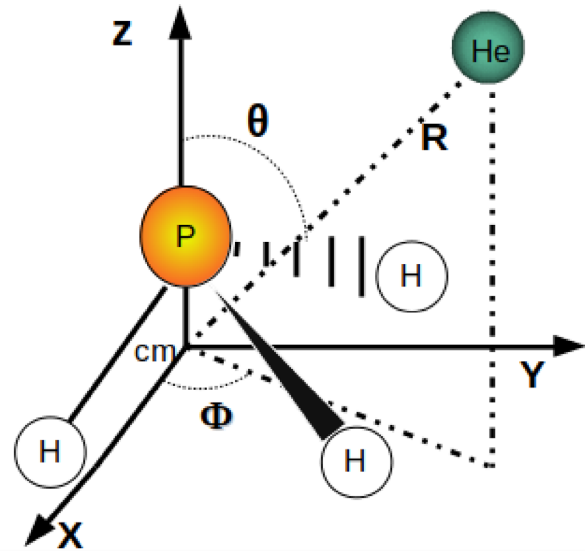


Figure 1. Description of the body-fixed coordinate system used in the calculations; cm stands for the centre of the PH_3 molecule.

an analytic expansion of the 3D-PES was obtained by fitting the computed energies. Later on, this 3D-PES is incorporated into time-independent quantum nuclear motion treatments to obtain the collision cross-sections and the collision rates after thermal averaging. Both ortho- and para- PH_3 were considered. As said above, the present set of data can be used to estimate the abundances of phosphine better and to model phosphorus chemistry in astrophysical media.

2 GENERATION OF THE 3D POTENTIAL ENERGY SURFACE OF PH_3 – HE

2.1 Potential energy surface

The system of interest (PH_3 – He) results from the interaction between a symmetric top molecule and a structureless atom in their ground electronic states, $\text{PH}_3(\tilde{X}^1A_1)$ and $\text{He}(^1S)$ respectively. The phosphine monomer was held fixed in its spatial configuration, as recommended by Faure et al. (2005), i.e. using the geometries of the vibrationless state. Typically, the distance between phosphorus (P) and each hydrogen (H) atom was set to $r_{\text{PH}} = 1.421 \text{ \AA}$ and the angle $\text{HPH} = 93.3^\circ$ (Herzberg 1966).

Taking into account the relatively large electron number of the titled system, it is desirable to reduce the number of degrees of freedom in the construction of the interaction potential, while keeping its efficiency in yielding accurate dynamic results. For the inelastic scattering of NH_3 due to He impact, neglecting umbrella inversion motion in the potential construction – as a model treatment – has led to errors in the amplitudes of the resonance peaks of less than 10 per cent relative to those obtained via a more elaborate treatment, where this motion was considered fully in the interacting PES (Gubbels et al. 2012). These errors in the amplitudes are rather small. At first glance, one can omit this motion. Consequently, the complex can be described in the PH_3 body-fixed (Jacobi) coordinate system using three parameters: (i) the distance (R) between mass of phosphine, (ii) the angle (θ), which stands for the rotation of He relative to the z -axis, and (iii) the rotation of PH_3 (Φ) with respect to the projection of the collision axis on the xy -plane (see Fig. 1). Therefore, the 3D-PES was constructed using 42 values of R ranging from 4 to $40a_0$, 19 He orientations

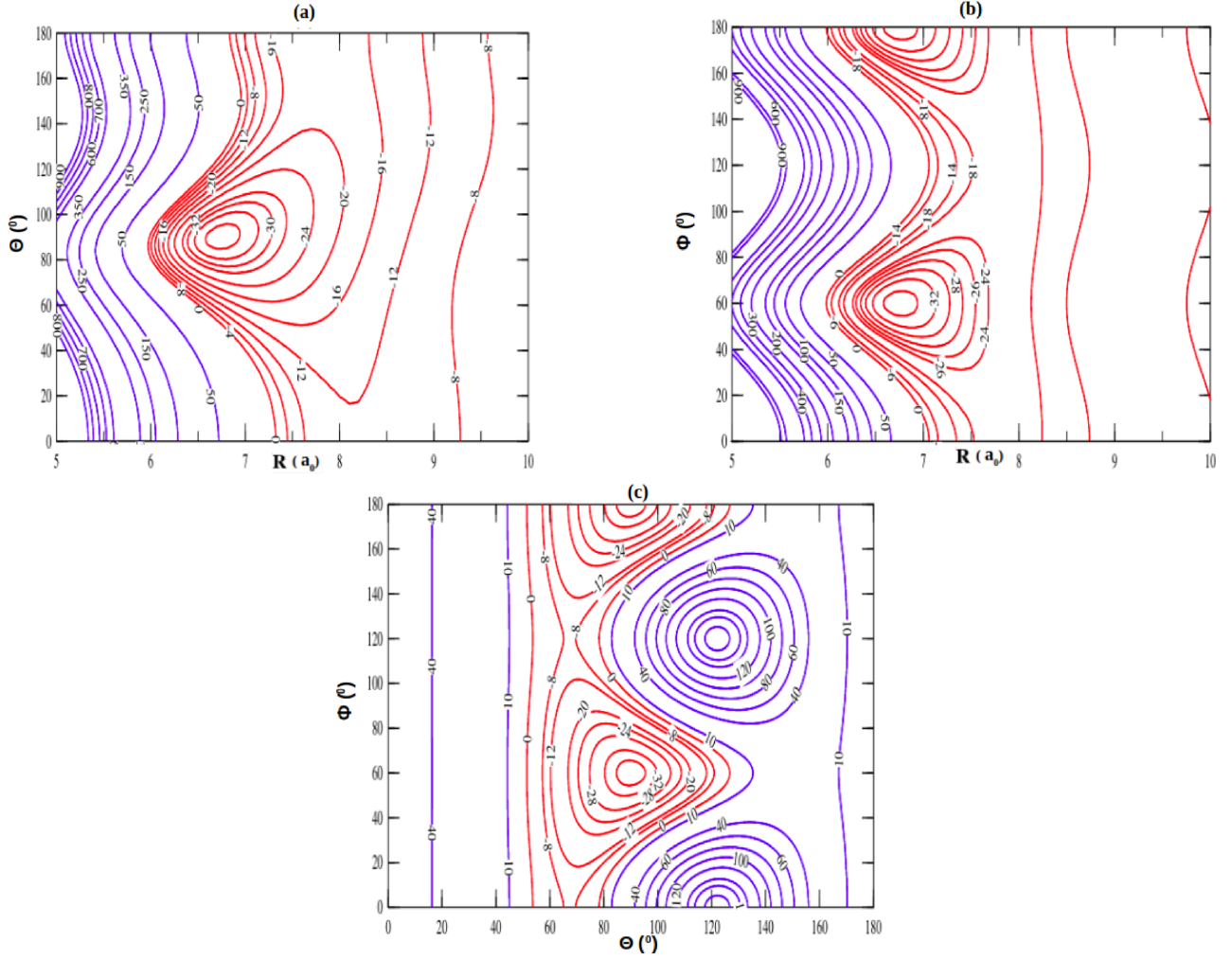


Figure 2. Two-dimensional contour plots of the three-dimensional potential energy surface of the PH_3 –He van der Waals complex. Panels (a), (b) and (c) depict respectively the 3D-PES as a function of θ and R at $\Phi = 60^\circ$, Φ and R at $\theta = 90^\circ$, and θ and Φ at $R = 6.75 a_0$. For each panel, the blue (red) contours represent the positive (negative) parts of the potential (in units of cm^{-1}). The reference energy is taken as that of the separated monomers.

($0^\circ \leq \theta \leq 180^\circ$) and seven Φ angles in the range $[0-60^\circ]$. All these parameters have led to a set of 5586 non-redundant nuclear configurations for which we performed *ab initio* electronic structure computations using the MOLPRO molecular package (Werner et al. 2010). Also, we used symmetry considerations to deduce the energies of the nuclear geometries not covered by our grid of points.

The 3D-PES was calculated using the coupled cluster with single, double and non-iterative triple excitations (CCSD(T)) method (Watts, Gauss & Bartlett 1993) in conjunction with the augmented-consistent correlation-polarized valence triple zeta (aug-cc-pVQZ) Gaussian basis sets of Dunning and co-workers (Dunning 1989), supplemented by the bond functions (bf) of Cybulski & Toczyłowski (1999). These latter (3s3p2d2f1g) were placed at mid-distance between the two monomers. This level of theory will be denoted thereafter as CCSD(T)/aug-cc-pVQZ+bf. In addition, we used the counterpoise procedure of Boys & Bernardi (1970) to correct for the basis set superposition errors (BSSE) using the following expression:

$$V(R, \theta, \Phi) = E_{\text{PH}_3-\text{He}}(R, \theta, \Phi) - E_{\text{PH}_3}(R, \theta, \Phi) - E_{\text{He}}(R, \theta, \Phi). \quad (1)$$

The accuracy of the interaction potentials generated using the methodology elaborated above has been assessed in our previous works (Najar et al. 2017; El Hanini et al. 2019).

We display in Fig. 2 the two-dimensional cuts of the 3D-PES of the PH_3 –He weakly bound system as a function of two Jacobi coordinates, whereas the third one was kept fixed at its equilibrium value in the PH_3 –He minimum. Indeed, we give the 3D-PES as a function of θ and R at $\Phi = 60^\circ$, Φ and R at $\theta = 90^\circ$ and θ and Φ for $R = 6.75$ bohr. The positive parts of the 3D-PES are in blue and the negative ones are in red, where the reference energy is taken as that of the separated PH_3 and He species. In terms of anisotropy, the interaction between helium and phosphine exhibits a relatively strong anisotropy.

Fig. 2 shows that the 3D-PES has a unique potential well of 34.92 cm^{-1} , which occurs at $\theta = 90^\circ$, $\Phi = 60^\circ$ and $R = 6.75$ bohr. This minimum is found at the same coordinates in Fig. 2(a) and (b), where the 2D cuts are periodical with a period of 120° relative to the Φ -axis, as expected for this C_{3v} symmetry molecule. Minimal energy configurations thus correspond to an He atom located between two H atoms and in the plane parallel to that formed by the three H atoms, whereas maxima of the potential occur where the He is in the plane containing the P, H bond and C_3 axis.

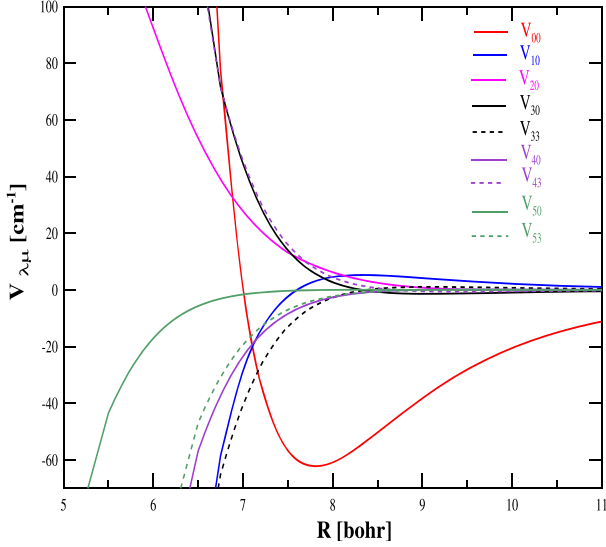


Figure 3. Dependence of selected radial coefficients (in units of cm^{-1}) with respect to R .

2.2 Analytic fit

In order to derive the radial coefficients $V_{\lambda\mu}(R)$ required for the dynamical calculations, we expanded the 3D-PES of $\text{PH}_3\text{-He}$ over the normalized spherical harmonic functions $Y_{\lambda\mu}(\theta, \Phi)$ as follows:

$$V(R, \theta, \Phi) = \sum_{\lambda\mu} V_{\lambda\mu}(R) Y_{\lambda\mu}(\theta, \Phi). \quad (2)$$

Due to the C_{3v} symmetry of the phosphine molecule, only radial terms for which $\mu = 3n$ (n being integer) are involved in the expansion (equation 2); the others are vanishing. Therefore, using the cubic spline routine, 70 radial coefficients ($0 \leq \lambda \leq 18$ and $0 \leq \mu \leq 18$) were needed to reproduce the *ab initio* potential reasonably within relative errors less than 5 per cent.

Fig. 3 depicts the variation of some radial coefficients (V_{00} , V_{10} , V_{20} , V_{30} , V_{33} , V_{40} and V_{43}) along the R Jacobi coordinate. The V_{00} , V_{20} , V_{30} and V_{43} terms have upward concavities, while the others are oriented downward. A close examination of this figure reveals that, for $\mu = 0$, the term related to $\lambda = 3$ outweighs the others with respect to the isotropic radial coefficient, namely V_{00} . This is also the case for $\mu = 3$ and $\lambda = 4$. Therefore, no clear predominance pattern can be associated with the index pair $\lambda\mu$. This lack of well-defined propensity scheme will have consequences on the behaviour of cross-sections. The radial coefficients derived from the $\text{NH}_3\text{-He}$ interacting potential show similar patterns, except for the terms involving $\mu = 3$ (Gubbels et al. 2012). Typically, the terms V_{33} and V_{43} are oriented downward and upward (upward and downward) for $\text{PH}_3\text{-He}$ ($\text{NH}_3\text{-He}$), respectively (i.e. they even present differences in sign at short range, as can be seen by comparison with fig. 3 of Gubbels et al. 2012).

3 DYNAMICAL CALCULATIONS

In this work, we are interested in the study of the rotational energy transfer of PH_3 after collision with He. PH_3 is a symmetric top rotor type molecule. Usually, j_k^ϵ is used to label the energy levels of such molecules, where the quantum number j stands for the total angular momentum and k its projection over the C_3 axis, while $\epsilon = \pm$ denotes the symmetry index. For a given rotational energy level, the parity of the rotation-inversion wavefunction and

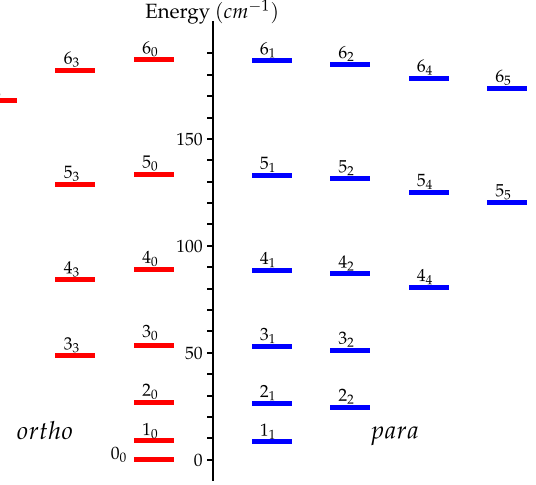


Figure 4. Diagram of the PH_3 rotational energy levels (E_{jk}). The energies are labelled as j_k . See text for the definition of these two quantum numbers. Their energies are given in Tables S1 and S2 in the Supplementary Material.

Table 1. Parameters used in the dynamical calculations to solve the coupled equations by means of the log derivative propagator. DTOL and OTOL stand for diagonal tolerance and off-diagonal tolerance, respectively.

ortho: $j_k^\epsilon = 16_1^0$	para: $j_k^\epsilon = 14_1^0$
$R_{\min} = 3a_0$	$R_{\max} = 35a_0$
STEPS = 10–200	$\mu = 3.581 \text{ au}$
DTOL = 0.01 \AA^2	OTOL = 0.005 \AA^2

the symmetry of the umbrella inversion are $(-1)^{j+k+1}\epsilon$ and $(-1)^{j+1}\epsilon$, respectively (Rist, Alexander & Valiron 1993). Due to the C_{3v} symmetry of the PH_3 molecule, the three hydrogen atoms of phosphine are identical in terms of spatial configuration. Thus, the rotational levels are split into ortho- PH_3 (o- PH_3) and para- PH_3 (p- PH_3), which stand for $k = 3n$ and $k \neq 3n$ (n being integer), respectively. As k can take any value except multiples of 3, the p- PH_3 rotational energy levels are denser than the o- PH_3 ones (see Fig. 4). These energy levels can be calculated using the spectroscopic constants $A = B = 4.4524 \text{ cm}^{-1}$ and $C = 3.919 \text{ cm}^{-1}$ by means of equation (3), where $\hbar^2/2I_x = X$ (Stroup, Oetjen & Bell 1953):

$$E_{jk} = \frac{\hbar^2}{2I_b} j(j+1) + \left(\frac{\hbar^2}{2I_c} - \frac{\hbar^2}{2I_b} \right) k^2. \quad (3)$$

As the conversion o- PH_3 to p- PH_3 (and vice versa) is forbidden, the ortho and para scattering channels are treated separately in the cross-section computations.

3.1 Cross-sections

The quantum nuclear treatment detailed in this section was performed with the MOLSCAT computer code (Hutson & Green 1994) using the time-independent close coupling method (Arthurs & Dalgarno 1960), along with the log derivative propagator (Manolopoulos 1986). Preliminary tests were done in order to fix the parameters of the propagator (see Table 1), such as the integration boundaries (R_{\min} and R_{\max}), the size of the rotational basis (j_{\max} and k_{\max}) and the integration step, which depends on the variable STEPS. These optimized values have been selected within a convergence threshold of 1.0 per cent \AA^2 . Thereafter, the total energy (E) was smoothly

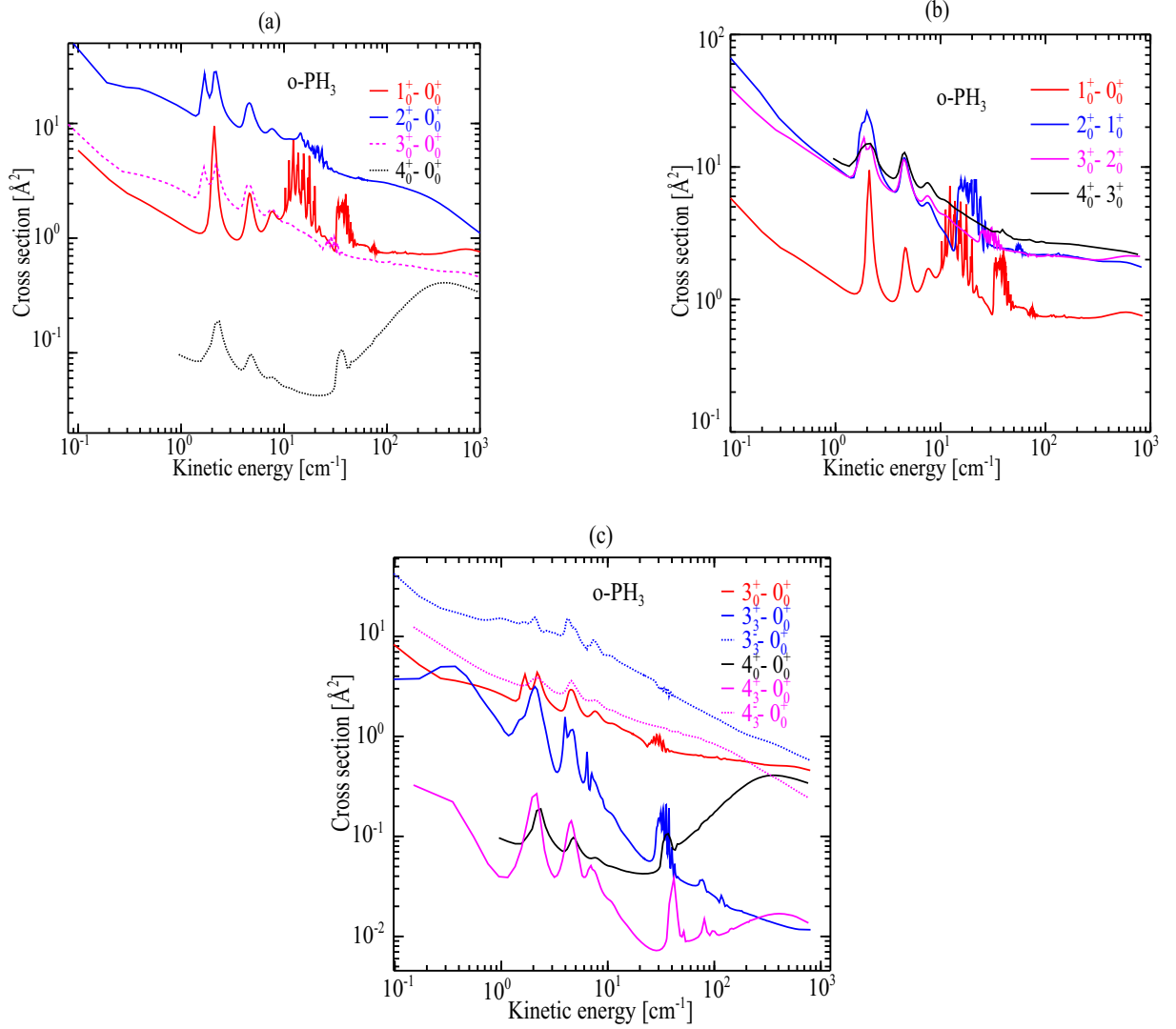


Figure 5. Inelastic cross-sections of $o\text{-PH}_3$, induced by collision with He, versus the kinetic energy; panels (a), (b) and (c) are for de-excitations involving selected low-lying rotational levels.

varied from $9\text{--}1000\text{ cm}^{-1}$ ($8.4\text{--}500\text{ cm}^{-1}$) for the scattering of $o\text{-PH}_3$ ($p\text{-PH}_3$). In order to converge cross-sections properly, we take all open channels into account by adding some closed channels for both ortho and para. The convergence tests showed that a rotational basis set including 97 levels for $o\text{-PH}_3$ is large enough. The 97th level corresponds to $j_{\text{max}} = 16$. For $p\text{-PH}_3$, we considered a basis set of 152 levels, corresponding to $j_{\text{max}} = 14$.

Fig. 5 displays the variation of cross-sections for $o\text{-PH}_3$ with respect to the kinetic energy. Fig. 5(a) depicts the $j_0^+ \rightarrow 0_0^+$ transitions, Fig. 5(b) represents the transitions for which $\{\Delta j, k, \epsilon\} = \{1, 0, +\}$ and Fig. 5(c) shows the $j_k^\epsilon \rightarrow 0_0^+$ transitions. All these curves, except those associated with the $4_0^+ \rightarrow 0_0^+$ and $4_1^- \rightarrow 1_1^+$ transitions, are decreasing while increasing the kinetic energy. Below 100 cm^{-1} , these cross-sections present both Feshbach and shape resonances. Such features were expected, as they were found in previous works, such as the one treating the collisional excitation of NH_3 by atomic and molecular hydrogen (Bouhafs et al. 2017) and that investigating the collisions between NH_3 and He (Machin & Roueff 2005). In fact, quasi-bound states occur when the He projectile is caught in the potential well, leading to Feshbach resonances. Regarding the shape resonances, they manifest

when tunnelling effects via the centrifugal energy barrier take place, forming quasi-bound states.

3.1.1 $o\text{-PH}_3$

Fig. 5(a) shows that the cross-sections of the $2_0^+ \rightarrow 0_0^+$ and $4_0^+ \rightarrow 0_0^+$ transitions are the strongest and weakest ones, respectively, in terms of magnitude, while an inversion occurs between the $1_0^+ \rightarrow 0_0^+$ and $3_0^+ \rightarrow 0_0^+$ transition cross-sections. Therefore, no selection rules can be associated with the parity of j . From Fig. 5(a) and (b), one can see that the magnitude of resonances decreases when j increases. Fig. 5(c) shows that the cross-sections of the $3_3^- \rightarrow 0_0^+$ ($4_3^- \rightarrow 0_0^+$) and $3_3^- \rightarrow 0_0^+$ ($4_3^- \rightarrow 0_0^+$) transitions are from either side of the $3_0^+ \rightarrow 0_0^+$ ($4_0^+ \rightarrow 0_0^+$) transition. Referring to each $j_0^+ \rightarrow 0_0^+$, the cross-sections of the $j_3^- \rightarrow 0_0^+$ transitions are lifted, while those of the $j_3^+ \rightarrow 0_0^+$ ones are shifted downward. Therefore, the propensity rule is in favour of symmetry (or parity) breaking, i.e. $\Delta k = 3$ and $j \rightarrow 0$. In addition, each cross-section for the $j_0^+ \rightarrow 0_0^+$ transition takes the shape of that of the $j_3^- \rightarrow 0_0^+$ transition at low kinetic energy and then switches progressively to that of $j_3^+ \rightarrow 0_0^+$.

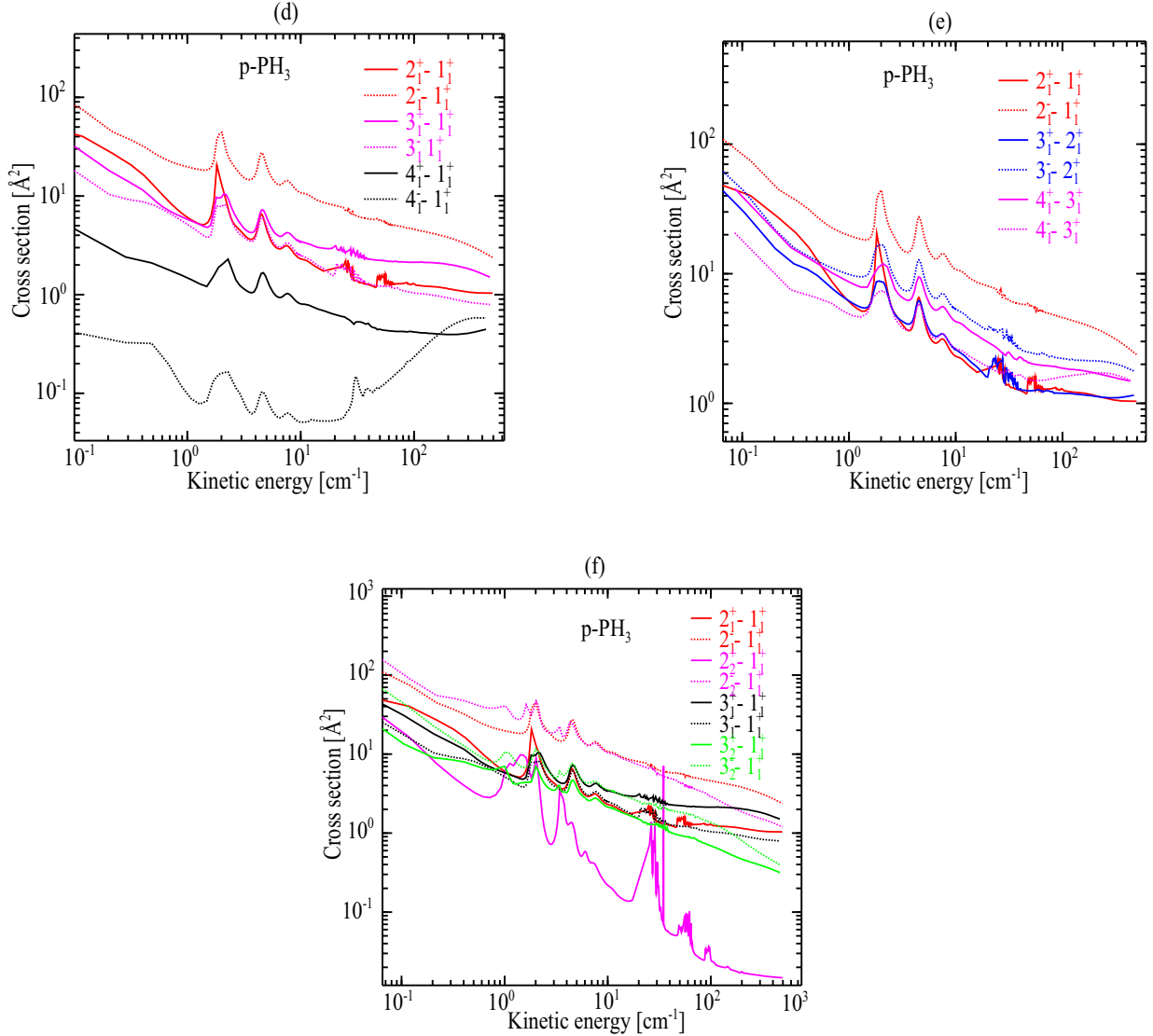


Figure 6. Inelastic cross-sections of p-PH₃ induced by collision with He versus kinetic energy; panels (a), (b) and (c) are for de-excitations involving selected low-lying rotational levels.

3.1.2 *p*-PH₃

Fig. 6 displays the variation of cross-sections for p-PH₃ with respect to the kinetic energy. Fig. 6(a) shows that the magnitude of cross-sections decreases when j increases for the $j_1^- \rightarrow 1_1^+$ transitions, while for the $j_1^+ \rightarrow 1_1^+$ transitions no net dominance is observed. In Fig. 6(b), all cross-sections have almost the same shape, whatever the transition, with typically the same location of resonance peaks. Regarding the magnitudes, the transitions involving negative parities are stronger than the corresponding ones with positive parities, except for $j = 4$. For instance, the cross-section of $2_1^- \rightarrow 1_1^+$ ($4_1^+ \rightarrow 3_1^+$) transition outweighs that of $2_1^+ \rightarrow 1_1^+$ ($4_1^- \rightarrow 3_1^+$). Thus, one can state the predominance of parity breaking; $\Delta k = 0$ and $\Delta j = 1$ is lifted for higher j values. Fig. 6(c) is an extension of Fig. 6(b) to show the effect of the change of Δk . The previously highlighted behaviour persists, but for fixed j and ϵ . The slight dominance of $k = 2$ occurs only at low kinetic energy, then it reverses at higher energies (e.g. the $2_1^- \rightarrow 1_1^+$ and $2_2^- \rightarrow 1_1^+$ transitions).

In summary, we can conclude that no general propensity rule can be associated with the indexes j, k, ϵ , in line with the already noticed behaviours of the radial coefficients (see Fig. 3).

3.2 Rate coefficients

In order to deduce the rotational rate coefficients ($R_{jk\epsilon \rightarrow j'k'\epsilon'}$) of both o-PH₃ and p-PH₃, we averaged the cross-sections discussed above thermally using the Maxwell–Boltzmann velocity distribution:

$$R_{\alpha \rightarrow \alpha'}(T) = \left(\frac{8}{\pi \mu \beta} \right)^{1/2} \beta^2 \int_0^\infty E_c \sigma_{\alpha \rightarrow \alpha'}(E_c) e^{-\beta E_c} dE_c, \quad (4)$$

where the kinetic energy is denoted by E_c , β stands for the reverse of $(k_B \times T)$, with k_B being the constant of Boltzmann, and α refers to $jk\epsilon$.

The cross-sections of ortho-PH₃ covering the range 9–1000 cm⁻¹ allow us to generate the velocity coefficient for the transitions

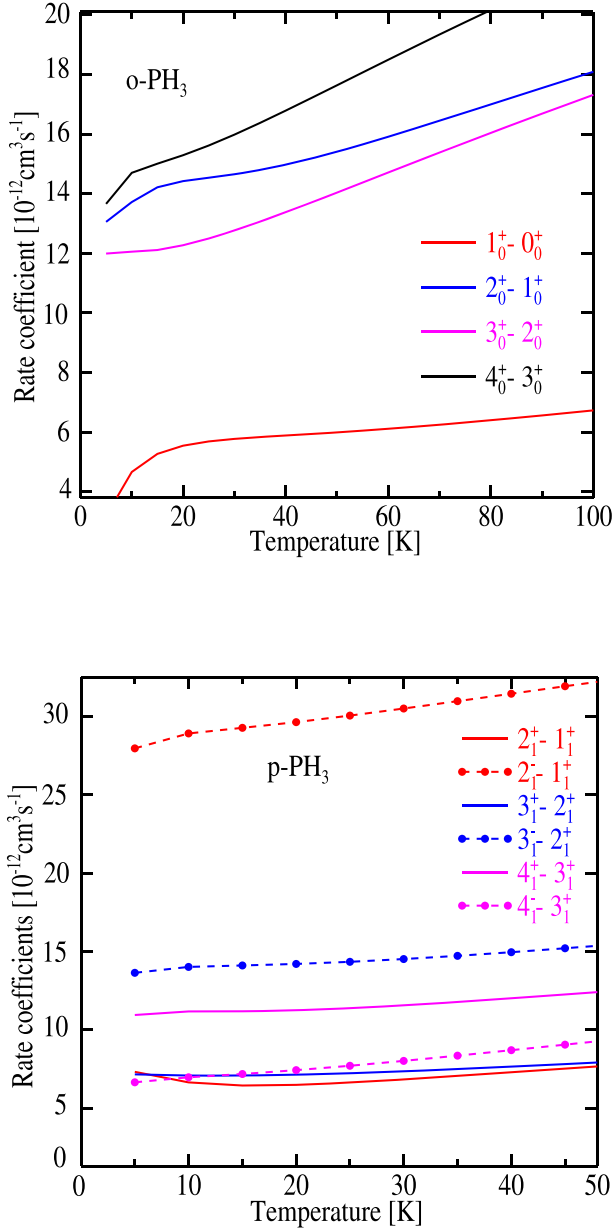


Figure 7. Downward rotational rate coefficients of o-PH₃ (top panel) and p-PH₃ (bottom panel) induced by collision with He, as a function of the kinetic temperature.

between the 41 low-lying rotational levels [up to $j_k = 10_0$] for temperatures up to 100 K. Similarly, the cross-sections of para-PH₃ covering the range 8.4–500 cm⁻¹ allow us to generate the velocity coefficient for the transitions between the 41 low-lying rotational levels [up to $j_k = 7_1$] for temperatures up to 50 K.

Fig. 7 displays the variation of rate coefficients for the rotational excitation of o-PH₃ and p-PH₃ due to collisions with He as a function of the kinetic temperature. We represented only a few curves, as the patterns observed for the cross-sections persist here, whereas the full set of data is given in the Supplementary Material. Typically, for o-PH₃, the top panel of Fig. 7 reproduces the behaviour observed in Fig. 5(b). The main difference consists of the dominance of the $4_0^+ \rightarrow 3_0^+$ transition, which occurs for the whole temperature range, and no inversion is observed among the $2_0^+ \rightarrow 1_0^+$ and $3_0^+ \rightarrow 2_0^+$ transitions. Regarding p-PH₃, the bottom panel of Fig. 7 confirms

Table 2. Comparison of PH₃ (this work) and NH₃ (Machin & Roueff 2005) rotational rate coefficients (in units of cm³ s⁻¹) at selected temperatures. The brackets stand for negative powers of ten.

Initial levels			Final levels			$T = 50$ K		$T = 100$ K	
j	k	ϵ	j'	k'	ϵ'	o-PH ₃	o-NH ₃	o-PH ₃	o-NH ₃
1	0	+	0	0	+	5.99(12)	2.72(12)	6.73(12)	4.65(12)
2	0	+	0	0	+	2.09(11)	1.37(11)	2.34(11)	1.72(11)
2	0	+	1	0	+	1.54(11)	0.59(11)	1.81(11)	0.88(11)
3	3	-	0	0	+	1.43(11)	1.19(11)	1.34(11)	1.45(11)
3	3	-	2	0	+	3.20(11)	1.61(11)	3.21(11)	2.36(11)
3	3	+	0	0	+	3.70(13)	0.11(13)	2.80(13)	0.14(13)
3	3	+	2	0	+	2.24(11)	0.23(11)	2.15(11)	0.45(11)
4	0	+	3	0	+	1.76(11)	0.66(11)	2.17(11)	0.98(11)
4	0	+	0	0	+	6.82(13)	1.76(13)	1.66(12)	3.61(13)
4	3	+	0	0	+	7.40(14)	1.51(14)	1.00(13)	0.25(13)

						$T = 25$ K		$T = 50$ K	
j	k	ϵ	j'	k'	ϵ'	p-PH ₃	p-NH ₃	p-PH ₃	p-NH ₃
2	2	+	1	1	+	2.61(13)	0.81(13)	2.23(13)	0.54(13)
2	2	-	1	1	+	2.70(11)	1.39(11)	2.57(11)	1.70(11)
2	1	+	1	1	+	6.63(12)	3.10(12)	7.76(12)	3.98(12)
2	1	-	1	1	+	3.01(11)	3.20(11)	3.24(11)	3.47(11)
3	2	+	1	1	+	5.60(12)	1.98(12)	5.58(12)	2.60(12)
3	2	-	1	1	+	9.75(12)	0.19(12)	1.02(11)	0.14(11)
3	1	+	2	1	+	7.23(12)	3.56(12)	7.98(12)	4.61(12)
3	1	-	2	1	+	1.43(11)	1.08(11)	1.55(11)	1.26(11)
4	1	+	3	1	+	1.14(11)	0.41(11)	1.25(11)	0.54(11)
4	1	-	3	1	+	7.71(12)	3.77(12)	9.41(12)	0.52(12)

the dominance in favour of the de-excitations for which the parity is broken, $\Delta k = 0$ and $j \leq 3 \rightarrow j'$, as can be seen in panel (e) of Fig. 5.

It is worth noting that the rate coefficients of NH₃ induced by collisions with helium (Machin & Roueff 2005), supplemented by those due to para-H₂ impact (Rist et al. 1993), were used to model the PH₃ abundance in astrophysical media. In this realm, comparing our data on PH₃-He with those of Machin & Roueff (2005) on NH₃-He is a clue to settle the validity of using rate coefficients of isoelectronic molecules instead. For this purpose, Table 2 compares the PH₃ rate coefficients computed in this work with those of NH₃ (Machin & Roueff 2005). This table shows that large differences between both sets of data are observed for both ortho and para, especially for $j \geq 3$. For $\Delta j = 1$ (as in the observed transitions, $1_0^+ \rightarrow 0_0^+$, $2_0^+ \rightarrow 1_0^+$ and $2_1^\epsilon \rightarrow 1_1^\epsilon$), we noticed agreement within a factor of ~ 2.5 . In order to have a global view of the comparison, in Fig. 8 we plot the rate coefficients of PH₃ as a function of those of NH₃. For both ortho and para, the data reported by Machin & Roueff (2005) are smaller than the values computed in this work. At low temperature, the rate coefficients of NH₃ can drop down to a factor of two orders of magnitude lower than those of PH₃. This discrepancy decreases as the temperature increases, which suggests a better agreement at higher temperatures ($T \geq 300$). Although PH₃ is observed in a relatively hot environment (e.g. the carbon star envelopes IRC+10216 and CRL2688), using the rate coefficients of NH₃ to model its abundance will lead to an underestimation of its density. Consequently, this may lead to misunderstandings in phosphorous chemistry, as phosphine is likely one of the main phosphorous reservoirs in space. Otherwise, the observed lines suggest that phosphine can be formed anywhere in a disc of radius $100R_*$ around the centre of the star (Agúndez et al. 2014). Hence, PH₃ can eventually be observed in warm/cold media, where the use of NH₃ rate coefficients would yield underestimation of the abundance of phosphine by a factor larger than one order of magnitude. Consequently, the present data should be used, rather than those of NH₃, for more reliable determination of the PH₃ abundances in space.

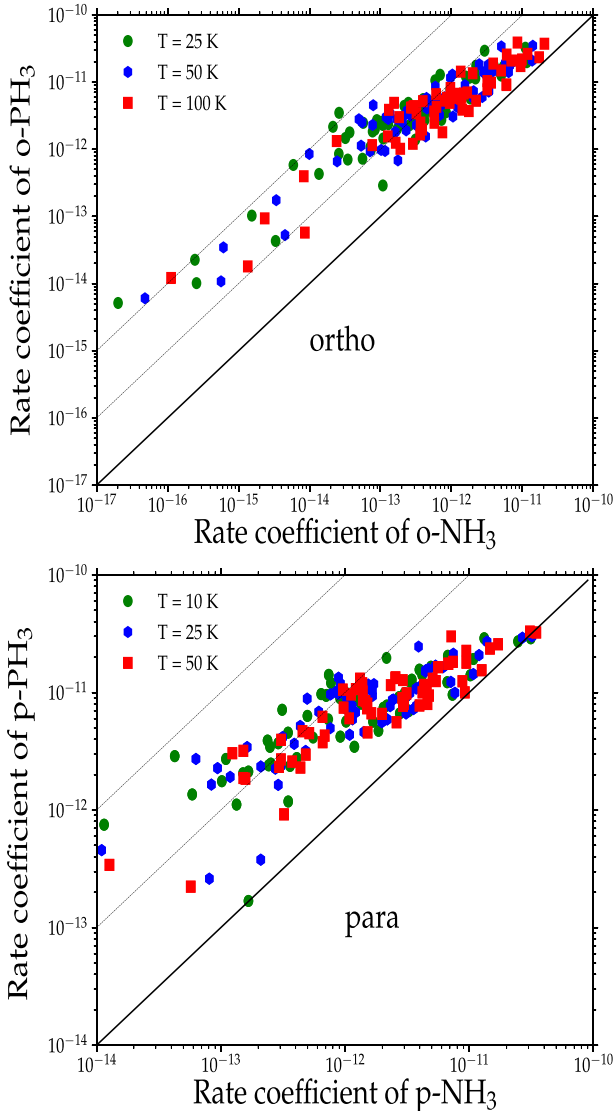


Figure 8. Comparison of the PH_3 rate coefficients (in cm^3s^{-1}) with those of NH_3 . With respect to the diagonal, the first dashed line represents a factor of one order of magnitude and the second dashed line stands for a factor of two orders of magnitude.

4 CONCLUSION

We carried out the construction of a highly accurate 3D-PES for the $\text{PH}_3\text{-He}$ interacting system. This 3D-PES was mapped in Jacobi coordinates and computed at the CCSD(T)/aug-cc-pVQZ+bf level of theory. The interaction among helium and phosphine is quite anisotropic and presents one single potential well of 34.92 cm^{-1} at $R = 6.75\text{ bohr}$, $\theta = 90^\circ$ for $\Phi = 60^\circ$ and $\Phi = 180^\circ$. Then, an analytical expansion of this 3D-PES was derived. These electronic structure computations were followed by computations of state-to-state inelastic cross-sections of rotational (de-)excitation of ortho- and para-phosphine, induced by collision with helium. This is done using a quantum mechanical treatment, by means of the close-coupling approach. These data were then thermally averaged according to the Maxwell-Boltzmann kinetic energy distribution, leading to record rate coefficients up to (100 K) 50 K for the (41) 42 low-lying rotational levels of (o- PH_3) p- PH_3 . No general propensity rules are found for either p- PH_3 or o- PH_3 .

The rate coefficients computed in this work were compared with those of Machin & Roueff (2005) for the $\text{NH}_3\text{-He}$ system, which is used to estimate the abundances of phosphine. Large differences are noticed, especially at low temperatures. Therefore, the results obtained in this work may be of great help to the astrophysical community, in order to model the physical conditions of media where phosphine was observed. Indeed, exact knowledge of the PH_3 abundance may be a clue to constrain the chemistry of interstellar phosphorus. In addition, the present data may help in the identification of PH_3 in astrophysical media where other P-containing molecules were detected, e.g. in massive dense cores (Fontani et al. 2016) or the Galactic Centre (Rivilla et al. 2018).

ACKNOWLEDGEMENTS

The authors acknowledge the Programme National ‘Physique et Chimie du Milieu Interstellaire’ (PCMI) of Centre National de la Recherche Scientifique (CNRS).

DATA AVAILABILITY

Collision rates are available in the Supplementary Material. The strongest inelastic transitions are of the order of 10^{-11} ; we considered as significant only values of rates that are greater than 1×10^{-14} . Values that are less than 1×10^{-14} are considered significantly zero.

REFERENCES

- Agúndez M., Cernicharo J., Guélin M., 2007, *ApJ*, 662, L91
 Agúndez M., Cernicharo J., Pardo J., Guélin M., Phillips T., 2008, *A&A*, 485, L33
 Agúndez M., Cernicharo J., Decin L., Encrenaz P., Teyssier D., 2014, *ApJ*, 790, L27
 Altwegg K. B. H. B.-N.-A. E. A. O., 2016, *Science Advances*, 2, e1600285
 Arnett D., Arnett W. D., 1996, *Supernovae and Nucleosynthesis: An Investigation of the History of Matter, From the Big Bang to the Present*. Princeton University Press
 Arthurs A., Dalgarno A., 1960, 540
 Barlow M. et al., 2013, *Science*, 342, 1343
 Bop C. T., Hammami K., Niane A., Faye N., Jaïdane N., 2016, *MNRAS*, p. stw2809
 Bouhafs N., Rist C., Daniel F., Dumouchel F., Lique F., Wiesenfeld L., Faure A., 2017, *MNRAS*, 470, 2204
 Boys S. F., Bernardi F. D., 1970, *Molecular Physics*, 19, 553
 Bregman J. D. L. D. F., Rank D. M., 1975, *ApJ*, 202, L55
 Cernicharo J. et al., 2018, *ApJ*, 853, L22
 Chantzos J., Rivilla V. M., Vasyunin A., Redaelli E., Bizzocchi L., Fontani F., Caselli P., 2020, *A&A*, 633, A54
 Cybulski S. M., Toczyłowski R. R., 1999, *The Journal of Chemical Physics*, 111, 10520
 Danby G., Flower D., Valiron P., Schilke P., Walmsley C., 1988, *MNRAS*, 235, 229
 De Beck E., Kamiński T., Patel N., Young K., Gottlieb C., Menten K., Decin L., 2013, *A&A*, 558, A132
 Dunning T. H., Jr, 1989, *The Journal of Chemical Physics*, 90, 1007
 El Hanini H., Najjar F., Naouai M., Jaidane N.-E., 2019, *Physical Chemistry Chemical Physics*
 Faure A., Valiron P., Wernli M., Wiesenfeld L., Rist C., Noga J., Tennyson J., 2005, A full nine-dimensional potential-energy surface for hydrogen molecule-water collisions
 Fontani F., Rivilla V., Caselli P., Vasyunin A., Palau A., 2016, *ApJ*, 822, L30
 Gubbels K. B., Meerakker S. Y. V. D., Groenenboom G. C., Meijer G., Avoird A. V. D., 2012, *The Journal of Chemical Physics*, 136, 074301
 Guélin M., Cernicharo J., Paubert G., Turner B., 1990, *A&A*, 230, L9
 Halfen D., Clouthier D., Ziurys L. M., 2008, *ApJ*, 677, L101

Herzberg G., 1966, Van Nostrand, Reinhold, New York
 Hutson J., Green S., 1994, Collaborative computational project
 Jiménez-Serra I., Viti S., Quénard D., Holdship J., 2018, *ApJ*, 862, 128
 Larson H., Fink U., Smith H., Davis D., 1980, *ApJ*, 240, 327
 Larson H. P. F. U. T.-R. R., 1977, *ApJ*, 211, 972
 Levy A., Lacombe N., Tarrago G., 1994, *Journal of Molecular Spectroscopy*, 166, 20
 Machin L., Roueff E., 2005, *Journal of Physics B: Atomic, Molecular and Optical Physics*, 38, 1519
 Maciá E., 2005, *Chemical Society Reviews*, 34, 691
 Manolopoulos D., 1986, *The Journal of Chemical Physics*, 85, 6425
 Milam S., Halfen D., Tenenbaum E., Apponi A., Woolf N., Ziurys L., 2008, *ApJ*, 684, 618
 Moreno R., Marten A., Lellouch E., 2009, in AAS/Division for Planetary Sciences Meeting Abstracts# 41
 Najar F., Naouai M., Hanini H. E., Jaidane N., 2017, *MNRAS*, 472, 2919
 Pickett H., Poynter R., Cohen E., 1981, *Journal of Quantitative Spectroscopy and Radiative Transfer*, 26, 197
 Ridgway S., Wallace L., Smith G., 1976, *ApJ*, 207, 1002
 Rist C., Alexander M. H., Valiron P., 1993, *The Journal of Chemical Physics*, 98, 4662
 Rivilla V. et al., 2018, *MNRAS*, 475, L30
 Salem J., Bouanich J.-P., Walrand J., Aroui H., Blanquet G., 2005, *Journal of Molecular Spectroscopy*, 232, 247
 Sharp C. M., Burrows A., 2007, *ApJS*, 168, 140
 Sousa-Silva C., Al-Refaie A. F., Tennyson J., Yurchenko S. N., 2015, *MNRAS*, 446, 2337
 Stroup R. E., Oetjen R. A., Bell E. E., 1953, *JOSA*, 43, 1096
 Tenenbaum E., Ziurys L. M., 2008a, *ApJ*, 680, L121
 Tenenbaum E., Ziurys L. M., 2008b, *ApJ*, 680, L121
 Tenenbaum E., Woolf N., Ziurys L. M., 2007, *ApJ*, 666, L29
 Turner B., Bally J., 1987, *ApJ*, 321, L75
 Turner B., Tsuji T., Bally J., Guélin M., Cernicharo J., 1990, *ApJ*, 365, 569
 Watts J. D., Gauss J., Bartlett R. J., 1993, *The Journal of Chemical Physics*, 98, 8718

Weisstein E. W., Serabyn E., 1996, *Icarus*, 123, 23
 Werner H.-J. et al., 2010, see <http://www.molpro.net>
 Woosley S., 2002, *Rev. Mod. Phys.*, 74, 1015
 Ziurys L. M., 1987, *ApJ*, 321, L81

SUPPORTING INFORMATION

Supplementary data are available at *MNRAS* online.

Table S1: Rotational levels of ortho-PH₃.

Table S2: Rotational levels of para-PH₃.

Table S3: Rate coefficients (in units of cm³ s⁻¹, given as $A(B) = A \times 10^{-B}$) of ortho-PH₃ induced by collision with He as a function of the kinetic temperature, where (II), IF corresponds to (Initial), Final–Index).

Table S4: Rate coefficients (in units of cm³ s⁻¹, given as $A(B) = A \times 10^{-B}$) of ortho-PH₃ induced by collision with He as a function of the kinetic temperature, where (II), IF corresponds to (Initial), Final–Index).

Table S5: Rate coefficients (in units of cm³ s⁻¹, given as $A(B) = A \times 10^{-B}$) of para-PH₃ induced by collision with He as a function of the kinetic temperature, where (II), IF corresponds to (Initial), Final–Index).

Please note: Oxford University Press is not responsible for the content or functionality of any supporting materials supplied by the authors. Any queries (other than missing material) should be directed to the corresponding author for the article.

This paper has been typeset from a T_EX/L^AT_EX file prepared by the author.

List of astronomical key words (Updated on 2020 January)

This list is common to *Monthly Notices of the Royal Astronomical Society*, *Astronomy and Astrophysics*, and *The Astrophysical Journal*. In order to ease the search, the key words are subdivided into broad categories. No more than *six* subcategories altogether should be listed for a paper.

The subcategories in boldface containing the word ‘individual’ are intended for use with specific astronomical objects; these should never be used alone, but always in combination with the most common names for the astronomical objects in question. Note that each object counts as one subcategory within the allowed limit of six.

The parts of the key words in italics are for reference only and should be omitted when the keywords are entered on the manuscript.

General

editorials, notices
errata, addenda
extraterrestrial intelligence
history and philosophy of astronomy
miscellaneous
obituaries, biographies
publications, bibliography
sociology of astronomy
standards

Physical data and processes

acceleration of particles
accretion, accretion discs
asteroseismology
astrobiology
astrochemistry
astroparticle physics
atomic data
atomic processes
black hole physics
chaos
conduction
convection
dense matter
diffusion
dynamo
elementary particles
equation of state
gravitation
gravitational lensing: micro
gravitational lensing: strong
gravitational lensing: weak
gravitational waves
hydrodynamics
instabilities
line: formation
line: identification
line: profiles
magnetic fields
magnetic reconnection
(*magnetohydrodynamics*) MHD
masers
molecular data
molecular processes
neutrinos
nuclear reactions, nucleosynthesis, abundances
opacity
plasmas
polarization

radiation: dynamics
radiation mechanisms: general
radiation mechanisms: non-thermal
radiation mechanisms: thermal
radiative transfer
relativistic processes
scattering
shock waves
solid state: refractory
solid state: volatile
turbulence
waves

Astronomical instrumentation, methods and techniques

atmospheric effects
balloons
instrumentation: adaptive optics
instrumentation: detectors
instrumentation: high angular resolution
instrumentation: interferometers
instrumentation: miscellaneous
instrumentation: photometers
instrumentation: polarimeters
instrumentation: spectrographs
light pollution
methods: analytical
methods: data analysis
methods: laboratory: atomic
methods: laboratory: molecular
methods: laboratory: solid state
methods: miscellaneous
methods: numerical
methods: observational
methods: statistical
site testing
space vehicles
space vehicles: instruments
techniques: high angular resolution
techniques: image processing
techniques: imaging spectroscopy
techniques: interferometric
techniques: miscellaneous
techniques: photometric
techniques: polarimetric
techniques: radar astronomy
techniques: radial velocities
techniques: spectroscopic
telescopes

Astronomical data bases

astronomical data bases: miscellaneous
atlases
catalogues
surveys
virtual observatory tools

Software

software: data analysis
software: development
software: documentation
software: public release
software: simulations

Astrometry and celestial mechanics

astrometry
celestial mechanics
eclipses
ephemerides
occultations
parallaxes
proper motions
reference systems
time

The Sun

Sun: abundances
Sun: activity
Sun: atmosphere
Sun: chromosphere
Sun: corona
Sun: coronal mass ejections (CMEs)
Sun: evolution
Sun: faculae, plages
Sun: filaments, prominences
Sun: flares
Sun: fundamental parameters
Sun: general
Sun: granulation
Sun: helioseismology
Sun: heliosphere
Sun: infrared
Sun: interior
Sun: magnetic fields
Sun: oscillations
Sun: particle emission
Sun: photosphere
Sun: radio radiation
Sun: rotation
(*Sun:*) solar–terrestrial relations
(*Sun:*) solar wind
(*Sun:*) sunspots
Sun: transition region
Sun: UV radiation
Sun: X-rays, gamma-rays

Planetary systems

comets: general

comets: individual: . . .

Earth
interplanetary medium
Kuiper belt: general

Kuiper belt objects: individual: . . .

meteorites, meteors, meteoroids

minor planets, asteroids: general

minor planets, asteroids: individual: . . .

Moon
Oort Cloud
planets and satellites: atmospheres
planets and satellites: aurorae
planets and satellites: composition
planets and satellites: detection
planets and satellites: dynamical evolution and stability
planets and satellites: formation
planets and satellites: fundamental parameters
planets and satellites: gaseous planets
planets and satellites: general

planets and satellites: individual: . . .

planets and satellites: interiors
planets and satellites: magnetic fields
planets and satellites: oceans
planets and satellites: physical evolution
planets and satellites: rings
planets and satellites: surfaces
planets and satellites: tectonics
planets and satellites: terrestrial planets
planet–disc interactions
planet–star interactions
protoplanetary discs
zodiacal dust

Stars

stars: abundances
stars: activity
stars: AGB and post-AGB
stars: atmospheres
(*stars:*) binaries (*including multiple*): close
(*stars:*) binaries: eclipsing
(*stars:*) binaries: general
(*stars:*) binaries: spectroscopic
(*stars:*) binaries: symbiotic
(*stars:*) binaries: visual
stars: black holes
(*stars:*) blue stragglers
(*stars:*) brown dwarfs
stars: carbon
stars: chemically peculiar
stars: chromospheres
(*stars:*) circumstellar matter
stars: coronae
stars: distances
stars: dwarf novae
stars: early-type
stars: emission-line, Be
stars: evolution
stars: flare
stars: formation
stars: fundamental parameters
(*stars:*) gamma-ray burst: general
(*stars:*) **gamma-ray burst: individual: . . .**
stars: general
(*stars:*) Hertzsprung–Russell and colour–magnitude diagrams
stars: horizontal branch
stars: imaging
stars: individual: . . .
stars: interiors

stars: jets
 stars: kinematics and dynamics
 stars: late-type
 stars: low-mass
 stars: luminosity function, mass function
 stars: magnetars
 stars: magnetic field
 stars: massive
 stars: mass-loss
 stars: neutron
 (*stars:*) novae, cataclysmic variables
 stars: oscillations (*including pulsations*)
 stars: peculiar (*except chemically peculiar*)
 (*stars:*) planetary systems
 stars: Population II
 stars: Population III
 stars: pre-main-sequence
 stars: protostars
 (*stars:*) pulsars: general
 (*stars:*) **pulsars: individual: . . .**
 stars: rotation
 stars: solar-type
 (*stars:*) starspots
 stars: statistics
 (*stars:*) subdwarfs
 (*stars:*) supergiants
 (*stars:*) supernovae: general
 (*stars:*) **supernovae: individual: . . .**
 stars: variables: Cepheids
 stars: variables: Scuti
 stars: variables: general
 stars: variables: RR Lyrae
 stars: variables: S Doradus
 stars: variables: T Tauri, Herbig Ae/Be
 (*stars:*) white dwarfs
 stars: winds, outflows
 stars: Wolf–Rayet

Interstellar medium (ISM), nebulae

ISM: abundances
 ISM: atoms
 ISM: bubbles
 ISM: clouds
 (*ISM:*) cosmic rays
 (*ISM:*) dust, extinction
 ISM: evolution
 ISM: general
 (*ISM:*) HII regions
 (*ISM:*) Herbig–Haro objects

ISM: individual objects: . . .

(*except planetary nebulae*)
 ISM: jets and outflows
 ISM: kinematics and dynamics
 ISM: lines and bands
 ISM: magnetic fields
 ISM: molecules
 (*ISM:*) photodissociation region (PDR)
 (*ISM:*) planetary nebulae: general
 (*ISM:*) **planetary nebulae: individual: . . .**
 ISM: structure
 ISM: supernova remnants

The Galaxy

Galaxy: abundances
 Galaxy: bulge
 Galaxy: centre
 Galaxy: disc
 Galaxy: evolution
 Galaxy: formation
 Galaxy: fundamental parameters
 Galaxy: general
 (*Galaxy:*) globular clusters: general
 (*Galaxy:*) **globular clusters: individual: . . .**
 Galaxy: halo
 Galaxy: kinematics and dynamics
 (*Galaxy:*) local interstellar matter
 Galaxy: nucleus
 (*Galaxy:*) open clusters and associations: general
 (*Galaxy:*) **open clusters and associations: individual: . . .**
 (*Galaxy:*) solar neighbourhood
 Galaxy: stellar content
 Galaxy: structure

Galaxies

galaxies: abundances
 galaxies: active
 galaxies: bar
 (*galaxies:*) BL Lacertae objects: general
 (*galaxies:*) **BL Lacertae objects: individual: . . .**
 galaxies: bulges
 galaxies: clusters: general
galaxies: clusters: individual: . . .
 galaxies: clusters: intracluster medium
 galaxies: disc
 galaxies: distances and redshifts
 galaxies: dwarf
 galaxies: elliptical and lenticular, cD
 galaxies: evolution
 galaxies: formation
 galaxies: fundamental parameters
 galaxies: general
 galaxies: groups: general

galaxies: groups: individual: . . .

galaxies: haloes
 galaxies: high-redshift

galaxies: individual: . . .

galaxies: interactions
 (*galaxies:*) intergalactic medium
 galaxies: irregular
 galaxies: ISM
 galaxies: jets
 galaxies: kinematics and dynamics
 (*galaxies:*) Local Group
 galaxies: luminosity function, mass function
 (*galaxies:*) Magellanic Clouds
 galaxies: magnetic fields
 galaxies: nuclei
 galaxies: peculiar
 galaxies: photometry
 (*galaxies:*) quasars: absorption lines
 (*galaxies:*) quasars: emission lines
 (*galaxies:*) quasars: general

(galaxies:) **quasars: individual: . . .**
(galaxies:) quasars: supermassive black holes
galaxies: Seyfert
galaxies: spiral
galaxies: starburst
galaxies: star clusters: general

galaxies: star clusters: individual: . . .
galaxies: star formation
galaxies: statistics
galaxies: stellar content
galaxies: structure

Cosmology

(cosmology:) cosmic background radiation
(cosmology:) cosmological parameters
(cosmology:) dark ages, reionization, first stars
(cosmology:) dark energy
(cosmology:) dark matter
(cosmology:) diffuse radiation
(cosmology:) distance scale
(cosmology:) early Universe
(cosmology:) inflation
(cosmology:) large-scale structure of Universe
cosmology: miscellaneous
cosmology: observations
(cosmology:) primordial nucleosynthesis
cosmology: theory

Resolved and unresolved sources as a function of wavelength

gamma-rays: diffuse background
gamma-rays: galaxies
gamma-rays: galaxies: clusters
gamma-rays: general
gamma-rays: ISM
gamma-rays: stars
infrared: diffuse background
infrared: galaxies
infrared: general
infrared: ISM
infrared: planetary systems
infrared: stars
radio continuum: galaxies
radio continuum: general
radio continuum: ISM
radio continuum: planetary systems
radio continuum: stars
radio continuum: transients
radio lines: galaxies
radio lines: general
radio lines: ISM
radio lines: planetary systems
radio lines: stars
submillimetre: diffuse background
submillimetre: galaxies
submillimetre: general
submillimetre: ISM
submillimetre: planetary systems
submillimetre: stars
ultraviolet: galaxies

ultraviolet: general
ultraviolet: ISM
ultraviolet: planetary systems
ultraviolet: stars
X-rays: binaries
X-rays: bursts
X-rays: diffuse background
X-rays: galaxies
X-rays: galaxies: clusters
X-rays: general
X-rays: individual: . . .
X-rays: ISM
X-rays: stars

Transients

(transients:) black hole mergers
(transients:) black hole - neutron star mergers
(transients:) fast radio bursts
(transients:) gamma-ray bursts
(transients:) neutron star mergers
transients: novae
transients: supernovae
transients: tidal disruption events